

The origin of different morphology of internal oxide precipitates in ferritic and austenitic steels

Zhao Shen¹, Xiaoqin Zeng^{1*}, Shengchuan Wu^{2*}, Hongbing Yu³, Benjamin M. Jenkins⁴, Phani Karamched⁴, Michael P. Moody⁴, Jianqiang Zhang⁵, Sergio Lozano-Perez^{4*}

¹National Engineering Research Center of Light Alloy Net Forming and State Key Laboratory of Metal Matrix Composites, School of Materials Science and Engineering, Shanghai Jiao Tong University, Shanghai, 200240, China

²State Key Laboratory of Traction Power, Southwest Jiaotong University, Chengdu 610031, China

³Department of Engineering Science, University of Oxford, Parks Road, OX1 3PJ Oxford, UK

⁴Department of Materials, University of Oxford, Parks Road, OX1 3PH Oxford, UK

⁵School of Materials Science and Engineering, University of New South Wales, Sydney, NSW 2052, Australia

Abstract: The internal oxide precipitates were supposed to be spherical in Wagner's original theory, while the following research demonstrated that this assumption is an exception rather than the truth, which caused deviations in the application of this theory. In this study, the internal oxide precipitates have a needle-like and a near-spherical morphology in a Fe-9Cr ferritic and a Fe-17Cr-9Ni austenitic steels after exposure to 600 °C deaerated steam for 600 h, respectively. The nano-to-atomic scale characterization shows that the morphology of the internal oxide precipitates is controlled by the structure of the interfaces between the metal matrix and the internal oxide, while the interface structure is mainly affected by the crystallographic structure of the two phases and their orientation relationship. In addition, the internal oxide precipitation-induced volume expansion and the outward Fe diffusion-induced volume shrink occur simultaneously during the oxidation process. The stress status in the internal oxidation zone (IOZ) is the competing result of the two factors, which could dynamically affect the high-temperature oxidation. The results obtained in this study suggest that there is potential to control the distribution, morphology, and interface structure of the internal oxide precipitates by selecting appropriate base metal and internal oxide-forming element, in order to obtain better high-temperature oxidation-resistant materials.

Key words: Austenitic steel; Ferritic steel; Oxide precipitates; Phase boundary; Orientation relationship.

1. Introduction

Due to their decent price, good mechanical properties, and reasonable corrosion resistance, Fe-Cr ferritic and Fe-Cr-Ni austenitic steels have been extensively used as heat-resisting materials in the petrochemical industry, aerospace sector, conventional fossil fuel power plants, and nuclear power industry [1-5]. To further increase the thermal efficiency and reduce carbon emissions, increasing the operating temperatures has been a widely accepted strategy, especially in the power generation systems, where water is used as a heat transfer medium [6-12]. One of the most critical challenges for the increase of operating temperature would be the serious corrosion of the structural materials under the service environments, which is detrimental to the long-term safe running of the systems. As a result, particular attention should be paid to the corrosion of the ferritic and austenitic steels at elevated temperatures.

It is reported that both Fe-Cr ferritic and Fe-Cr-Ni austenitic steels are internally oxidized at elevated temperatures if the content of Cr in the matrix is lower than a critical value [13]. To date, the corrosion of Fe-Cr-Ni austenitic steels at elevated temperatures has been extensively studied [14-34]. A typical duplex oxide scale forms on the austenitic steels. Extensive studies on ferritic steels in literature have also revealed a duplex oxide scale after exposure to high-temperature environments [35-55]. The structure of the oxide scale is similar to that observed on austenitic steels. Tracer studies show that the interface between the outer and inner oxide layers coincides with the original surface of the coupon specimens [56-58]. Consequently, it was proposed that the growth of the outer oxide layer is due to the outward diffusion of Fe and the growth of the inner oxide layer is due to the inward diffusion of oxygen-induced internal oxidation [14-17].

Although the phenomenon of internal oxidation had been reported by many researchers for decades, it was not until 1959 that it was systematically analysed and formalized by C. Wagner, proposing a Wagner theory [13]. This theory provides a way to calculate the rate at which an alloy is penetrated by dissolved oxygen as it precipitates the more reactive alloying elements. Although it has been successfully used in predicting the internal oxidation rate of several binary alloys, deviations from this theory have also been frequently reported [4, 5, 59-66]. The deviations are mainly due to the assumptions made in the development of this theory, including stoichiometric oxides precipitated, all reactive elements consumed for oxide formation, uniform planar fronts existed, spherical internal oxide precipitates, a constant mole fraction of oxide existed across the reaction zone, etc. [66]. Among these assumptions, spherical internal oxide precipitates are not always correct [66, 67]. To date, various forms of internal oxide precipitates are reported, including Widmanstätten platelets, hexagonal plates, dendritic products, near-spherical particles, and needle-like plates, etc. [4, 5, 66]. The different morphologies of the internal oxide precipitates could affect the inward flux of oxygen to different extents, and then affect the corrosion resistance of the specific materials [66, 67]. To mitigate the materials corrosion at elevated temperatures, it is crucial to understand the fundamental mechanisms that govern the morphology of the internal oxide precipitates. Due to the difficulties in achieving required nano-to-atomic scale of observations of the nano-sized internal oxide precipitates, the mechanisms controlling the morphology of the internal oxide precipitates remain unclear and require further investigation.

In recent studies conducted by the authors' group, the corrosion of a Fe-17Cr-9Ni austenitic and a Fe-9Cr ferritic steels in 600°C steam have been revealed to be dominated by internal oxidation, while the morphologies of the internal oxide precipitates in the two steels are completely different [34, 36, 37, 68, 69]. Near-spherical oxide precipitates are uniformly distributed in the austenitic steel, while the

oxide precipitates in the ferritic steel appear to have needle-like morphology [34, 36, 37, 68, 69]. Recent developments in high-resolution microscopy techniques, enabling a more detailed characterization of material microstructure, have significantly advanced our understanding of a range of previously unresolved phenomena [70-73]. In this study, we use advanced characterization techniques to conduct a direct study on the internal oxide precipitates formed on a Fe-17Cr-9Ni austenitic and a Fe-9Cr ferritic steels after exposure to 600°C steam for the same amount of time. The unprecedented micro-to-atomic scale observations captured in this study and related simulation results will shed light on the formation mechanisms of different morphologies of the internal oxide precipitates in the two steels which is important for corrosion control of these alloys.

2. Experimental

The materials used in this study are a Fe-17Cr-9Ni austenitic and a Fe-9Cr ferritic steels, and their nominal compositions are shown in Table 1. Coupon specimens ($15 \times 10 \times 2 \text{ mm}^3$) were machined from the as-received plate materials, and then polished to 1.0 μm diamond paste, followed by 10 minutes of final treatment with colloidal silica to obtain mirror-finished surfaces. The surface morphologies of the coupons after polishing were examined by Forward Scatter Detector (FSD) imaging, and the results are shown in Figs. 1a and c. The crystallographic orientation of the coupons was analysed by Electron Back Scattered Diffraction (EBSD), and the inverse pole figures along the z-axis (IPFZ) are shown in Figs. 1b and d. The grain sizes are not uniform in both steels, rather coarse (20-120 μm) for Fe-17Cr-9Ni but very fine (5-25 μm) for Fe-9Cr. Although the microstructures of the surface oxide scales of these two materials after oxidation have been reported [34, 36], the corrosion times were different in those studies. For a more reliable comparison, the well-polished coupons in this study were simultaneously exposed to 600 °C deaerated steam for 600 h. More details about the high-temperature testing can also be found in [34, 36].

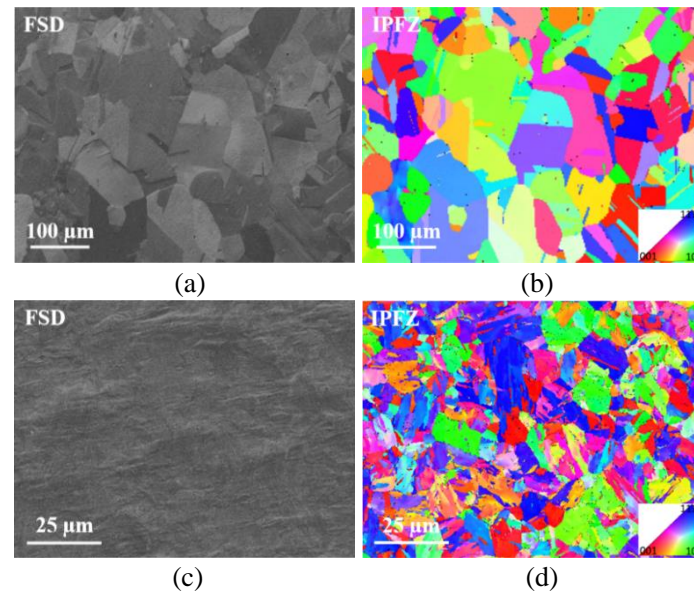


Fig. 1. EBSD analysis of the Fe-17Cr-9Ni and Fe-9Cr steels prior to corrosion testing (step size= 0.2 μm): (a) FSD and (b) IPFZ images of Fe-17Cr-9Ni austenitic steel; (c) FSD and (d) IPFZ images of Fe-9Cr ferritic steel.

Table 1. Nominal compositions of the two steels in this study (wt.%)

Materials	C	Cr	V	Si	Mn	Mo	P	S	Cu	Ni	Fe
Fe-17Cr-9Ni	0.082	16.91	0.049	0.18	-		0.022	<0.001	0.41	8.87	Bal.

Fe-9Cr	0.092	8.93	0.21	0.25	0.45	0.82	0.012	0.002	0.18	0.23	Bal.
--------	-------	------	------	------	------	------	-------	-------	------	------	------

The microstructure and chemical composition of the surface oxide scales of the two steels after reaction were characterized by a Zeiss Scanning Electron Microscope (SEM) equipped with Oxford Instruments Energy Dispersive X-ray (EDX) and EBSD detector systems. Site-specific Transmission Electron Microscope (TEM) thin foils were prepared by a dual beam Zeiss NVision 40 Focused Ion Beam (FIB). Higher resolution analyses on the TEM foils were conducted by a Zeiss Merlin SEM equipped with an Optimus Transmission Kikuchi Diffraction (TKD) detector and an aberration-corrected JEOL ARM200F TEM. Chemical composition analysis was conducted by Atom Probe Tomography (APT), using a LEAP 5000 XR.

3. Results

3.1 Microscale SEM-EBSD analysis of the surface oxide scales

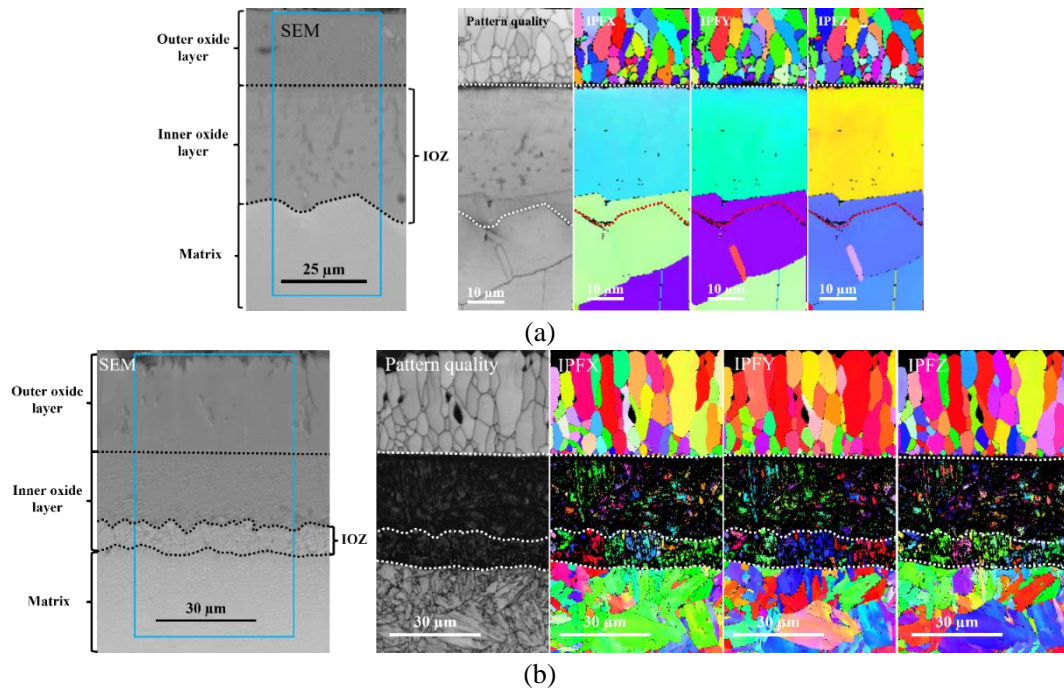


Fig. 2. SEM image and EBSD analysis results (from left to right: pattern quality, IPFX, IPFY, and IPFZ maps) of the surface oxide scale cross-sections of (a) Fe-17Cr-9Ni austenitic steel and (b) Fe-9Cr ferritic steel after exposure to 600°C steam for 600 h.

To eliminate the potential effect caused by the different reaction condition, the two steels were simultaneously exposed to the same autoclave for 600 h. Fig. 2 shows a typical SEM morphology and corresponding EBSD analysis results of the cross-sections of the oxide scales on the two steels. It is seen that the oxide scales on the two steels all have a duplex structure: an outer oxide layer and an inner oxide layer. EBSD analysis shows that the outer oxide layers of the two steels are composed of columnar oxide grains, while the inner oxide layers of the two steels appears to be different. The inner oxide layer of Fe-17Cr-9Ni steel retains the same crystallographic structure as the underneath metal matrix (Fig. 2a), which has been reported to be an internal oxidation zone (IOZ) [34]. The inner oxide layer of Fe-9Cr steel is not well-indexed, and an IOZ is observed at the oxidation front (Fig. 2b) [36].

3.2 Nanoscale TEM analysis of the internal oxide precipitates

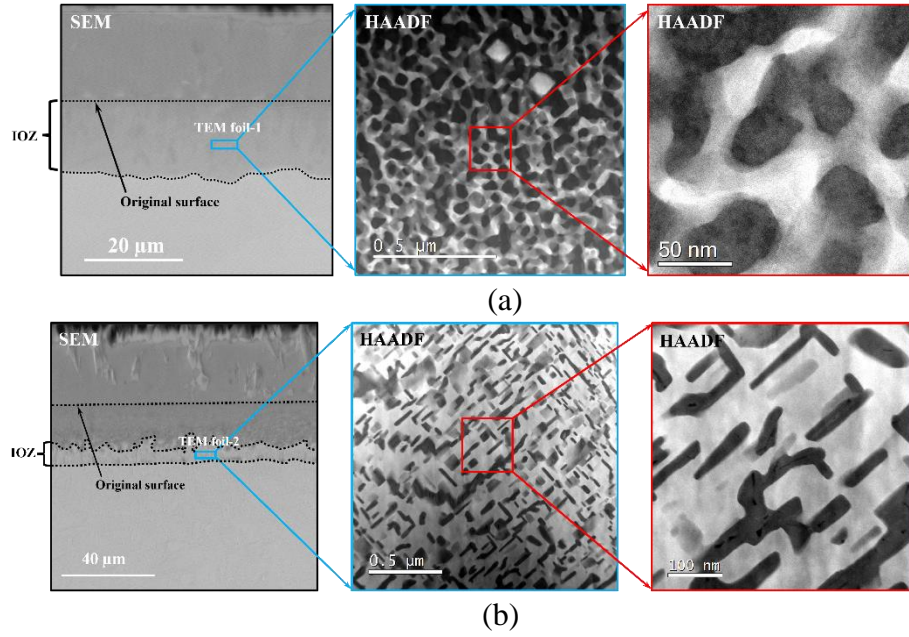


Fig. 3. Morphologies of the internal oxide layers under different scales of observation: (a) Fe-17Cr-9Ni austenitic steel; (b) Fe-9Cr ferritic steel.

Due to the small size of the internal oxide precipitates in the two steels, they cannot be observed under the microscale characterization (SEM images in Fig. 3). Hence, three TEM foils were prepared from each of the two steels for higher resolution analysis. Since the three TEM foils showed similar results, only the results from one typical TEM foil were presented. TEM foil 1 was prepared from the region shown in Fig. 3a for Fe-17Cr-9Ni steel. Since the High-Angle Annular Dark-Field (HAADF) imaging is sensitive to the average atomic number and specimen thickness, assuming a local uniform thickness of TEM foils prepared by FIB, it is easy to distinguish oxide from metal due to their different average atomic numbers. The HAADF images in Fig. 3a clearly reveal that the IOZ has not been fully oxidized, containing metal (in bright) and oxide (in dark) phases. TEM foil 2 was prepared from the region shown in Fig. 3b for Fe-9Cr steel. The HAADF images show that the IOZ of Fe-9Cr steel has also not been fully oxidized. The oxidation in the IOZs of the two steels has been shown to be in the form of oxide precipitation in the metal matrix [34, 36]. Since the microstructures of the oxide scales in Fe-17Cr-9Ni and Fe-9Cr steels are very similar to those in [34] and [36], respectively, it is reasonable to conclude that the exposure time should not change the oxidation mechanism of the two steels, at least during the oxidation periods in this study and in [34, 36], but may alter the kinetics. Although oxide precipitates are observed in the two alloys, their morphologies are different, near-spherical in Fe-17Cr-9Ni steel but needle-like in Fe-9Cr steel. Due to the different image contrasts of the oxide and metal phases in the HAADF images, the volume fraction of oxide precipitates in the internal oxide layer of Fe-17Cr-9Ni and Fe-9Cr steels are measured to be ~50% and ~34%, respectively. It is necessary to point out that due to the severe overlap between the oxide precipitates and metal matrix in Fe-17Cr-9Ni steel, the phase interfaces are difficult to be accurately identified. Hence, the approach used for the calculation of the volume fraction of oxide precipitates in Fe-17Cr-9Ni steel may be not very accurate.

3.3 Nanoscale TKD analysis of the internal oxide precipitates

TEM foil 2 in Fig. 3b was further analysed by TKD. Fig. 4a shows the Argus image collected by the Bruker EBSD detector. Although the oxide precipitates are in nano-sized, they can be clearly resolved

under this image. The needle-like oxide precipitates observed in Fig. 4a are very similar to those observed in 3b. Further observation shows that the growth of the needle-like precipitates appears to have two dominant directions, and the two directions are perpendicular to each other. The oxide precipitates and matrix are indexed as Face Centred Cubic (FCC) spinel and Body Centred Cubic (BCC) metal, respectively. The results are shown in Fig. 4b, in which the oxide precipitates and matrix are shown in green and red pixels, respectively. Fig. 4c shows the Kernel Misorientation (KMO) values in the matrix. It is clearly seen that the matrix surrounding the oxide precipitates has been preferentially deformed. The crystallographic orientations of the oxide precipitates and matrix along the x-, y-, and z-axis are shown in Fig. 4d. It is seen that the oxide precipitates in a same matrix grain do not have an identical crystallographic orientation.

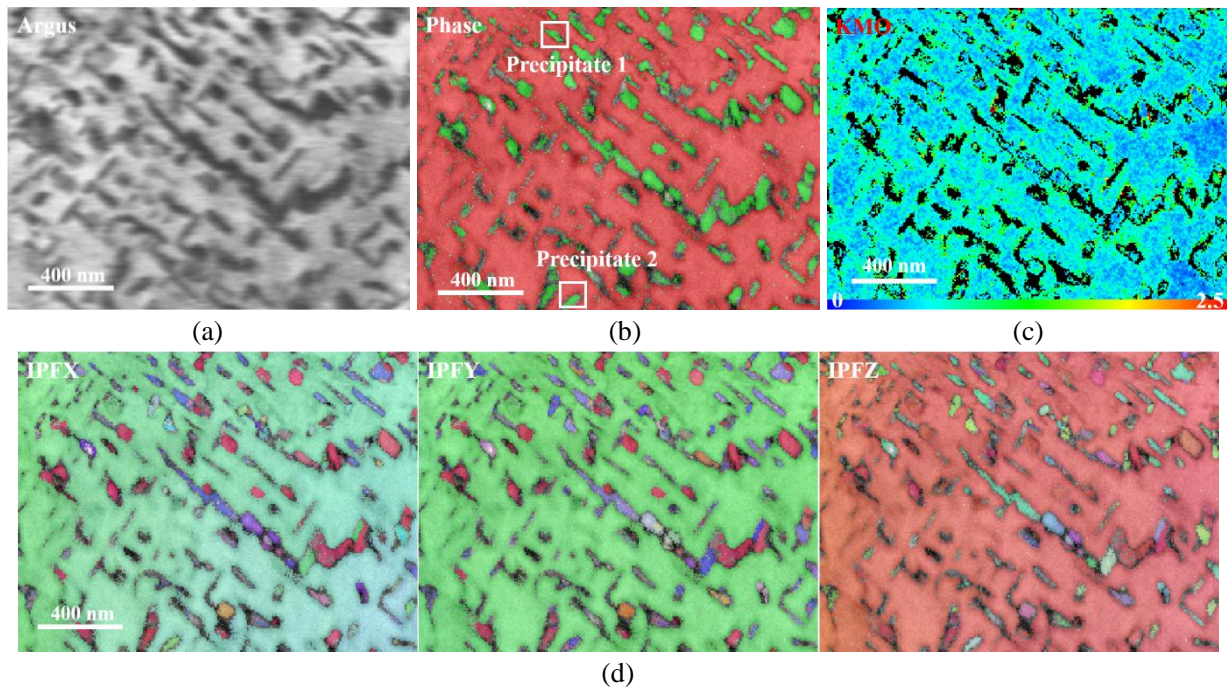


Fig. 4. TKD analysis on the internal oxide layer of Fe-9Cr ferritic steel (step size=5 nm, collected Kikuchi pattern resolution= 300×400). (a) Argus map; (b) phase map; (c) KMO map; (d) IPF maps.

To understand the orientation relationships between the oxide precipitates and their surrounding matrix, the pole figures of all the precipitates and their surrounding matrix are examined. Since the growth of the oxide precipitates has two dominant directions, two representative oxide precipitates are selected from the two dominant directions. The positions of the two selected precipitates are marked in Fig. 4b by white rectangles. The phase maps and related pole figures of the two precipitates and their surrounding matrix are shown in Fig. 5. It is seen that the two dominant growth directions all belong to $\langle 001 \rangle$ orientations. Further observation shows that the longer side of the phase boundaries are always parallel to (001) planes of both phases. Although the crystallographic orientations of the oxide precipitates are not the same, the pole figures show that the orientation relationships between the oxide precipitates and their surrounding matrix are the same, which is $(001)_{\text{metal}} // (001)_{\text{oxide}}$ and $[001]_{\text{metal}} // [110]_{\text{oxide}}$.

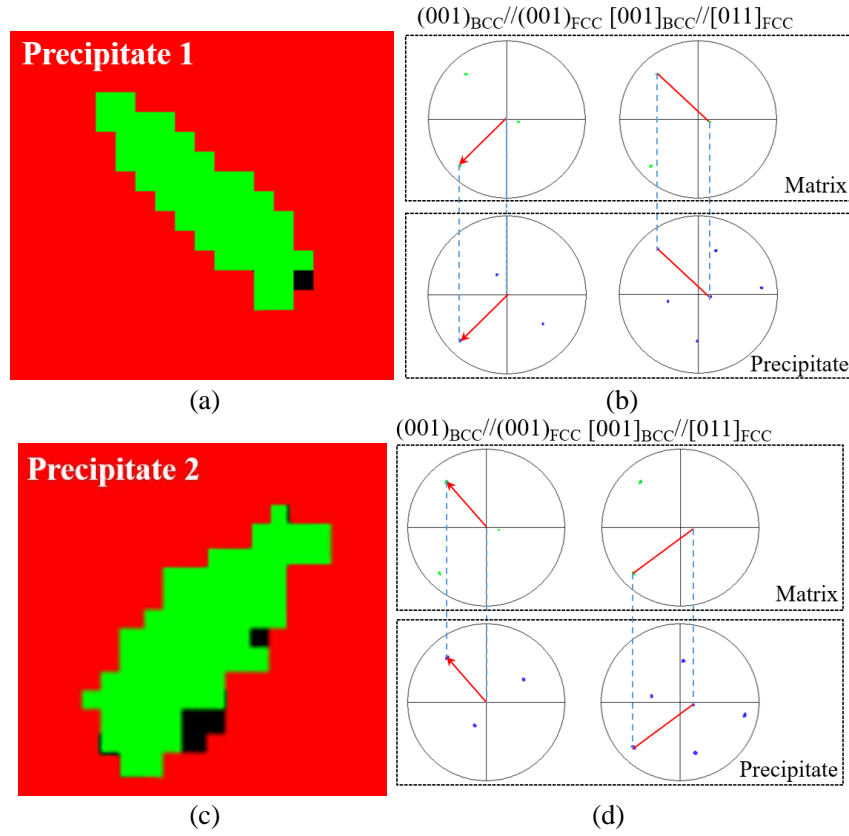


Fig. 5. Pole figures of the two typical oxide precipitates with their surrounding metal matrix (unindexed pixels shown in black) in Fe-9Cr ferritic steel. (a) Phase map of precipitate 1 in Fig. 4b and (b) related pole figures; (c) phase map of precipitate 2 in Fig. 4b and (d) related pole figures.

Due to the limited resolution of the collected Kikuchi patterns in Fig. 4, the preferential deformation observed in Fig. 4c can only be treated as qualitative. To quantify the extent of preferential deformation in the matrix surrounding the oxide precipitates, a high-resolution TKD analysis with a collected Kikuchi pattern resolution of 800×1200 was conducted. After the TKD Kikuchi pattern collection, the geometrically necessary dislocation (GND) density was calculated. The local orientations as determined from TKD in a regular grid of points were used to calculate orientation differences between neighbouring points and then in turn converted to a lattice curvature estimate. This method is based on the one suggested by Wilkinson et al. [74] and Pantleon [75] and built on the local dislocation density tensor introduced by Nye [76]. It is worth noting that the GND calculations in this work are not based on high-resolution cross-correlation but on a Hough-based indexing routine instead [77]. As shown in Fig. 6, the GND values in the matrix surrounding the oxide precipitates are about 1 to 2 orders of magnitude greater than that of the other regions, suggesting an enhanced deformation in the matrix surrounding the oxide precipitates.

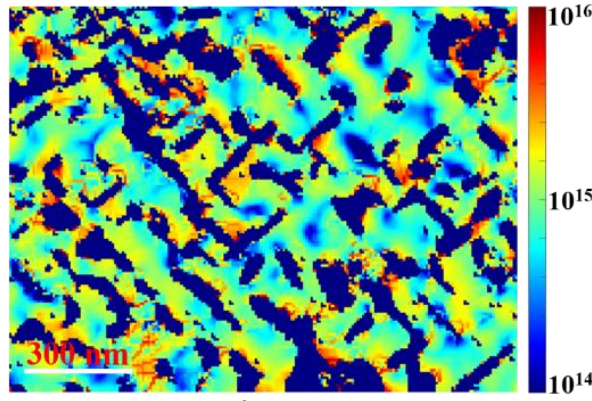


Fig. 6. Quantification of the GND values (m^{-2}) in the matrix phase of the internal oxide layer of Fe-9Cr ferritic steel (step size=5 nm, collected Kikuchi pattern resolution= 800×1200).

A similar TKD analysis approach was also applied to the analysis of TEM foil 1. Due to the relatively high density of oxide precipitates in this foil (~50%), the severe overlap between the two phases under TKD beam scanning results in a worse index quality. Hence, the crystallographic information of the oxide precipitates and their surrounding matrix could not be obtained via this approach.

3.4 Atomic-scale TEM analysis of the internal oxide precipitates

To examine the interfacial structures between the oxide precipitates and their surrounding matrix in Fe-17Cr-9Ni steel, atomic-scale HAADF imaging was conducted. One typical result is shown in Fig. 7a, in which the oxide is shown in dark and the metal in white. Fast Fourier Transform (FFT) patterns show that the metal phase is FCC austenite at [001] zone axis (Fig. 7b) and the oxide phase is FCC spinel at [001] zone axis (Fig. 7c). The FFT pattern in Fig. 7d is generated from the whole map of Fig. 7a. It is seen that the two phases have completely the same crystallographic orientation. The orientation relationship between the two phases can be described as $(001)_{\text{metal}} // (001)_{\text{oxide}}$ and $[001]_{\text{metal}} // [001]_{\text{oxide}}$. Although the two phases have the same crystallographic orientation, their lattice parameters are different. The lattice parameters of the metal and oxide phases are measured to be 3.56 and 8.30 Å, respectively. Due to the overlap between the two phases caused by the projected view of a tilted interface (Fig. 4a), a sharp interface image cannot be obtained from this sample. As shown in Fig. 7a, the overlap between the two phases around the interface prevents a clear observation of the interface structures. It is worth noting that to properly show the two phases in a single HAADF image, Fig. 7a has been manually rotated while the corresponding FFT images were generated from the original HAADF image.

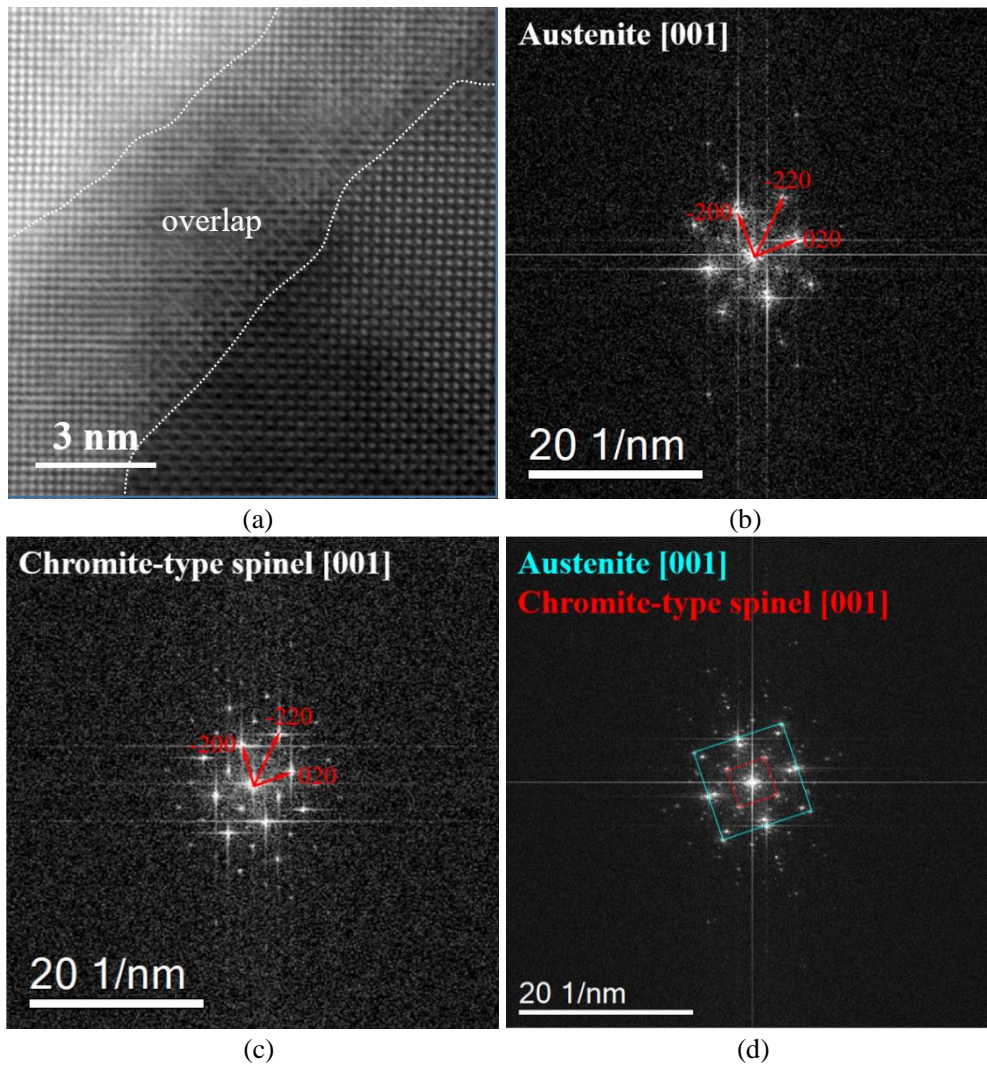


Fig. 7. (a) HAADF image showing the atomic structure of a typical oxide precipitate-metal interface of Fe-17Cr-9Ni austenitic steel; (b) FFT patterns of the metal phase in (a); (c) FFT patterns of the oxide phase in (a); (d) FFT patterns generated from the whole map in (a).

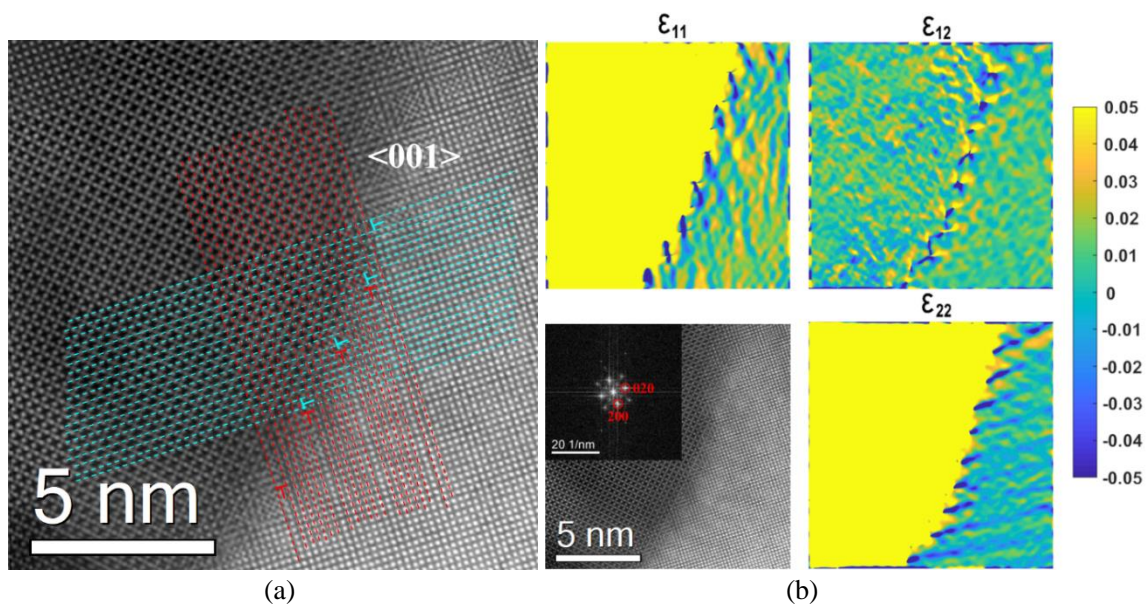


Fig. 8. (a) Atomic-scale HAADF image showing the oxide precipitate-metal interface structure of Fe-17Cr-9Ni austenitic steel after exposure to SCW for 1500h [34]; (b) GPA analysis results showing the distribution of horizontal (ϵ_{11}), vertical (ϵ_{22}), and shearing (ϵ_{12}) strains in the metal phase.

Although the precipitate-metal interface structure cannot be clearly observed in Fig. 7a, according to the results presented above, the oxidation mechanism of Fe-17Cr-9Ni steel after exposure to 600 °C steam for 600 h has also been shown to be internal oxidation. This is identical to that reported in [34], in which the same steel was oxidized for 1500 h in the same environment. Hence, the interface structure in the steel oxidized for 600 h is supposed to be the same to that oxidized for 1500 h [34]. As shown in Fig. 8a [34], the atomic structure of a reasonably sharp precipitate-metal interface can be observed. Although the two phases have the same crystallographic orientation, their different lattice parameters lead to the formation of a semi-coherent interface (every 7 continuous $\langle 001 \rangle$ planes in the metal phase take a dislocation to accommodate the misfit of the two phases). To evaluate the strain distribution in the metal phase surrounding the oxide precipitates, Geometric Phase Analysis (GPA) was conducted [78]. As shown in the FFT patterns of the metal phase (Fig. 8b), the (002) and (020) spots were chosen for the GPA analysis. The distribution of horizontal (ϵ_{11}), vertical (ϵ_{22}), and shearing (ϵ_{12}) strains are shown in Fig. 8b. The temperature bar indicates strain changes ranging from -0.05% to +0.05%. Periodical distribution of compressive and tensile strains at the phase boundary corresponds well with the distribution of lattice misfit dislocations at the phase interface. In addition, significant lattice distortions are observed in the matrix surrounding the precipitate. As a result, the growth of oxide precipitates in the matrix could introduce significant strains to the matrix surrounding them, which may affect the subsequent growth of the oxide precipitates [79]. It is worth noting that since the matrix surrounding the oxide precipitates may have been preferentially deformed, the reference used for the GPA calculation is not stress-free. It means that the strains measured from the GPA are relative values instead of absolute values. Hence, although the strains in the matrix are measured to be tensile strains, they are also possible to be compressive strains. The properties of the strains in the internal oxide layer will be discussed later.

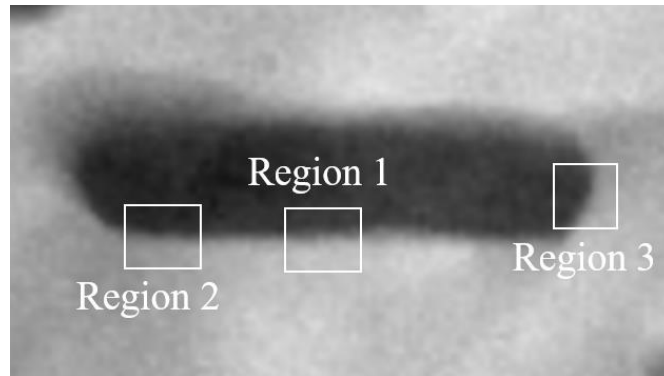


Fig. 9. HAADF image showing the morphology of a typical needle-like oxide precipitate in Fe-9Cr ferritic steel.

Fig. 9 shows the morphology of a typical needle-like oxide precipitate in Fe-9Cr steel. Considering its special geometry of the needle-shaped precipitate, the atomic structures of the phase interface at three different regions were examined. The atomic structure shown in Fig. 10a was observed around the middle part of the longer side phase boundary (Region 1 in Fig. 9). The FFT patterns demonstrate that the bright and dark phases are BCC metal (lattice parameter=2.91 Å) and FCC spinel (lattice

parameter=8.30 Å), respectively. The FFT patterns generated from the whole map of Fig. 10a clearly show that the longer side phase boundary is parallel to the (001) plane of both phases, which corresponds well with that observed from TKD analysis (Fig. 5).

Fig. 11a shows the atomic structure of the phase boundary at Region 2 in Fig. 9. The growth of the oxide precipitate on the plane of (001)_{metal}//(001)_{oxide} is also observed. The atomic structure of the phase boundary at the narrow side is shown in Fig. 11b (Region 3 in Fig. 9). It is seen that the morphology of the narrow side phase boundary is very different from that of the longer side. The growth of the oxide precipitate on a specific plane is not observed. In addition, many dislocation misfits are observed at the narrow side phase boundary.

Fig. 12 shows the GPA analysis results from the image in Fig. 10a. The (12-1) and (200) spots were chosen for this analysis. Significant lattice distortions are also observed in the matrix surrounding the oxide precipitate, which corresponds well with the GND analysis results in Fig. 6. Although the significant lattice distortions can still be observed, the quality of GPA results in Fig. 12 was much worse than that of Fig. 8, which is mainly attributed to the worse HAADF image in Fig. 10a.

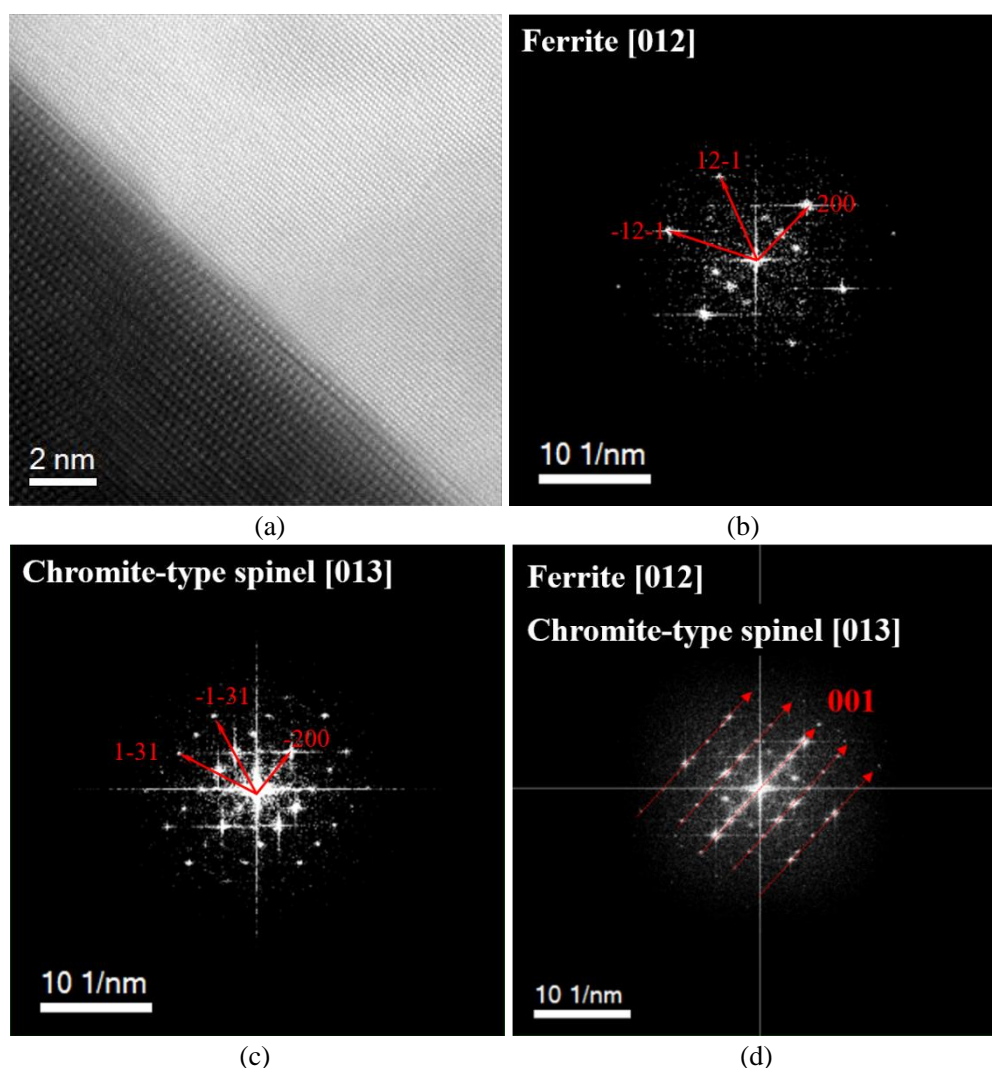


Fig. 10. (a) HAADF image showing the atomic structure of a typical oxide precipitate-metal interface of Fe-9Cr ferritic steel (Region 1 in Fig. 10); (b) FFT patterns of the metal phase in (a); (c) FFT patterns of the oxide phase in (a); (d) FFT patterns generated from the whole map in (a).

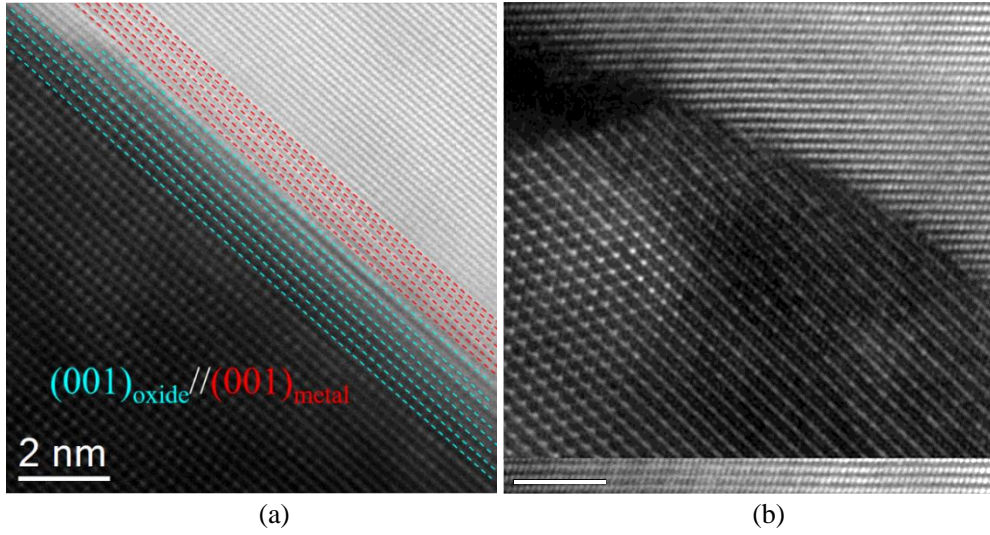


Fig. 11. Atomic-resolution HAADF images showing the structure of a typical oxide precipitate-metal interface of Fe-9Cr ferritic steel at (a) Region 2 and (b) Region 3 in Fig. 10.

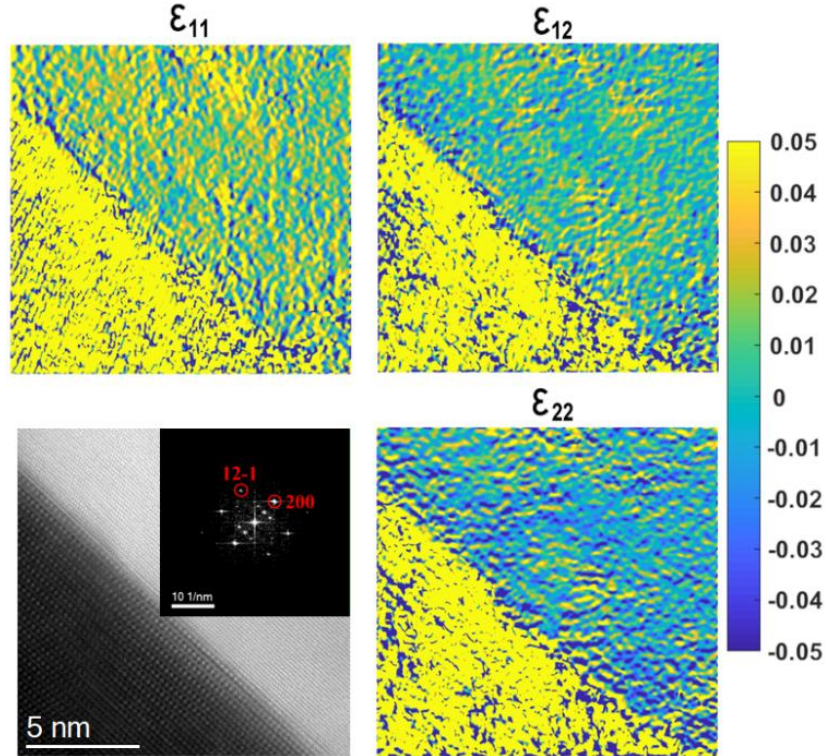


Fig. 12. GPA analysis results showing the distribution of horizontal (ϵ_{11}), vertical (ϵ_{22}), and shearing (ϵ_{12}) strains in the metal phase of Fe-9Cr ferritic steel.

3.5 Simulation of the oxide precipitate-matrix interface structure

The atomic-resolution images presented above can only show the cross-sectional morphologies of the phase boundaries. To obtain a more comprehensive understanding of the phase boundary structures, two-dimensional (2D) phase boundaries are reconstructed by superimposing the two phases based on the crystallographic information obtained in this study. The orientation relationship between the two phases in Fe-17Cr-9Ni steel has been identified as $(001)_{\text{metal}} // (001)_{\text{oxide}}$ and $[001]_{\text{metal}} // [001]_{\text{oxide}}$ (Fig. 7). Since the oxide precipitates in Fe-17Cr-9Ni steel have near-spherical shape (no preferential growth directions), the 2D phase boundary structures are examined by superimposing the two phases along two representative directions: $[001]_{\text{oxide}} // [001]_{\text{metal}}$ and $[100]_{\text{oxide}} // [100]_{\text{metal}}$, as shown in Fig. 13a. In

this simulation, the spinel oxide is modelled by FeCr_2O_4 , since both the EELS chemical composition analysis in this study (not shown) and in literature [34] shows an atomic ratio of Fe : Cr : O = 1 : 2 : 4. It is seen from Fig. 13a that the phase boundary structures along the two directions are completely the same. This observation could well explain the spherical morphology of the oxide precipitates in this steel since no preferential growth direction exists and the oxide precipitates grow equally towards all directions. It is worth noting that the simulated phase boundary structure in Fig. 13a is not completely the same with that observed from HAADF image (Fig. 8). This difference is because the simulation used in this study could only simulate the orientation relationship between the two phases and the dislocation misfits caused by their different lattice parameters cannot be accounted by the approach used here.

The orientation relationship between the two phases in Fe-9Cr steel has been identified as $(001)_{\text{metal}} // (001)_{\text{oxide}}$ and $[001]_{\text{metal}} // [110]_{\text{oxide}}$ (Fig. 5). In addition, the TKD pole figures (Fig. 5) and atomic-resolution images (Figs. 10 and 11) presented above show that the longer side phase boundaries always parallel to (001) planes of both phases. As shown in Fig. 13b, the phase boundary structures of the longer and narrow sides are simulated by superimposing the two phases along $[001]_{\text{oxide}} // [001]_{\text{metal}}$ and $[1-10]_{\text{oxide}} // [100]_{\text{metal}}$ directions. The oxide precipitates in this steel are also modelled by FeCr_2O_4 according to the results reported in this study and in [36]. It is seen that the two phases are completely coherent on the longer side phase boundary while they are incoherent on the narrow side. These results correspond well with the atomic-resolution images in Fig. 11. It is known that the growth of precipitates on coherent interfaces is much slower than on incoherent interfaces [80-82]. The acicular morphology of the internal oxide precipitates might be due to different growth rates along different directions. More details will be discussed later.

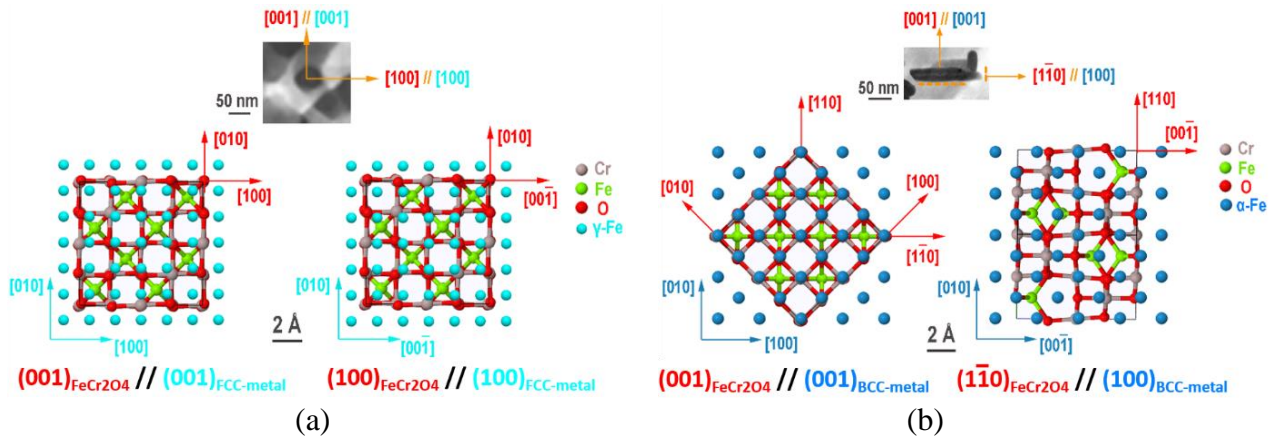


Fig. 13. Simulation of the atomic structures of 2D oxide precipitate-matrix phase boundaries in (a) Fe-17Cr-9Ni austenitic and (b) Fe-9Cr ferritic steels.

3.6 Atomic-scale APT analysis of the internal oxide precipitates

Due to the overlap between the oxide precipitates and their surrounding matrix, especially for Fe-17Cr-9Ni steel, it is difficult to obtain an accurate chemical composition distribution across the phase boundaries under TEM. In this study, the chemical composition distribution in the two phases was analysed by three-dimensional (3D) APT. Fig. 14a shows the distribution of ions in the APT needle prepared from the IOZ of Fe-17Cr-9Ni steel. It is seen that the oxide precipitates are mainly composed of O, Cr, Fe, and the metal phase mainly consists of Fe and Ni, which are consistent to EELS analysis results in [34]. Compared with EELS, another advantage of APT is that the 3D distribution of minor elements can also be obtained. The results show that the oxide precipitates are not pure FeCr_2O_4 and

some minor elements such as Mn, V, Si are also present. Cu, on the other hand, is mainly in the metal phase and slightly enriched at the phase boundaries. C is not enriched in any of the two phases but preferentially distributed at the phase boundaries. To quantify the chemical composition across the phase boundaries, a set of elemental line profiles are extracted (Fig. 14b). The atomic ratios of the major elements are consistent to those measured from EELS [34], and the enrichment of Cu and C at the phase boundaries is also confirmed from the line profiles.

An APT sample prepared from the IOZ of Fe-9Cr steel was also analysed. The distribution of ions is shown in Fig. 15a. It is seen that the oxide precipitates mainly consist of O, Cr, Fe, although Mn, V, and Si are also observed, indicating that the oxide precipitates in Fe-9Cr steel are also not pure FeCr_2O_4 [36]. The metal phase is mainly composed of Fe. Ni, Cu, and C are mainly distributed at the phase boundaries. A set of line profiles are also extracted to quantify the elemental distribution across the phase boundary. The atomic ratios of the major elements are also consistent to those measured from EELS [36], and the enrichment of Ni, Cu, and C at the phase boundaries is also confirmed from the line profiles (Fig. 15b).

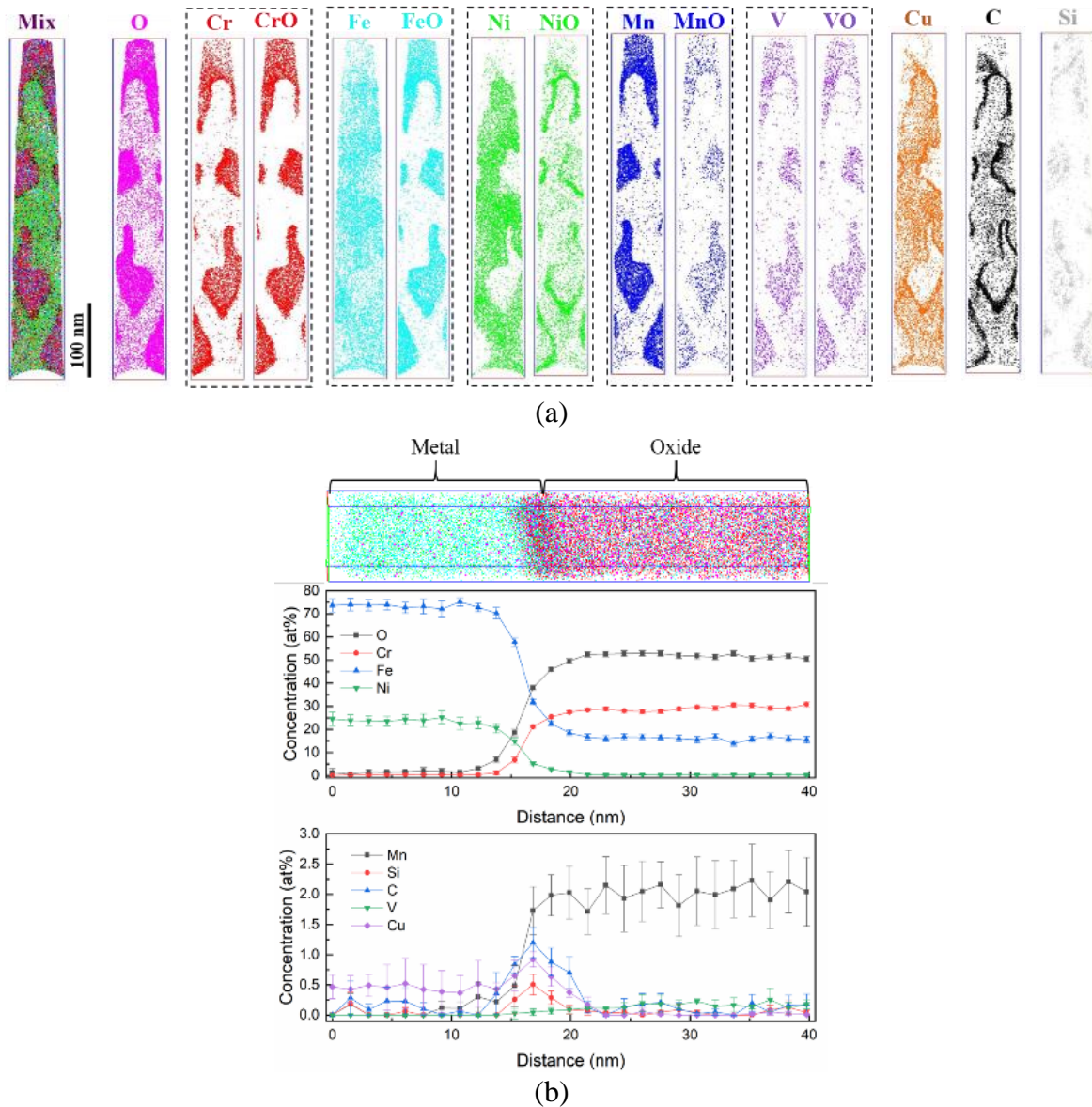


Fig. 14. (a) A representative region of Fe-17Cr-9Ni austenitic steel showing ion distributions (plane thickness ~ 5 nm); (b) Line profiles showing the quantitative elemental distribution.

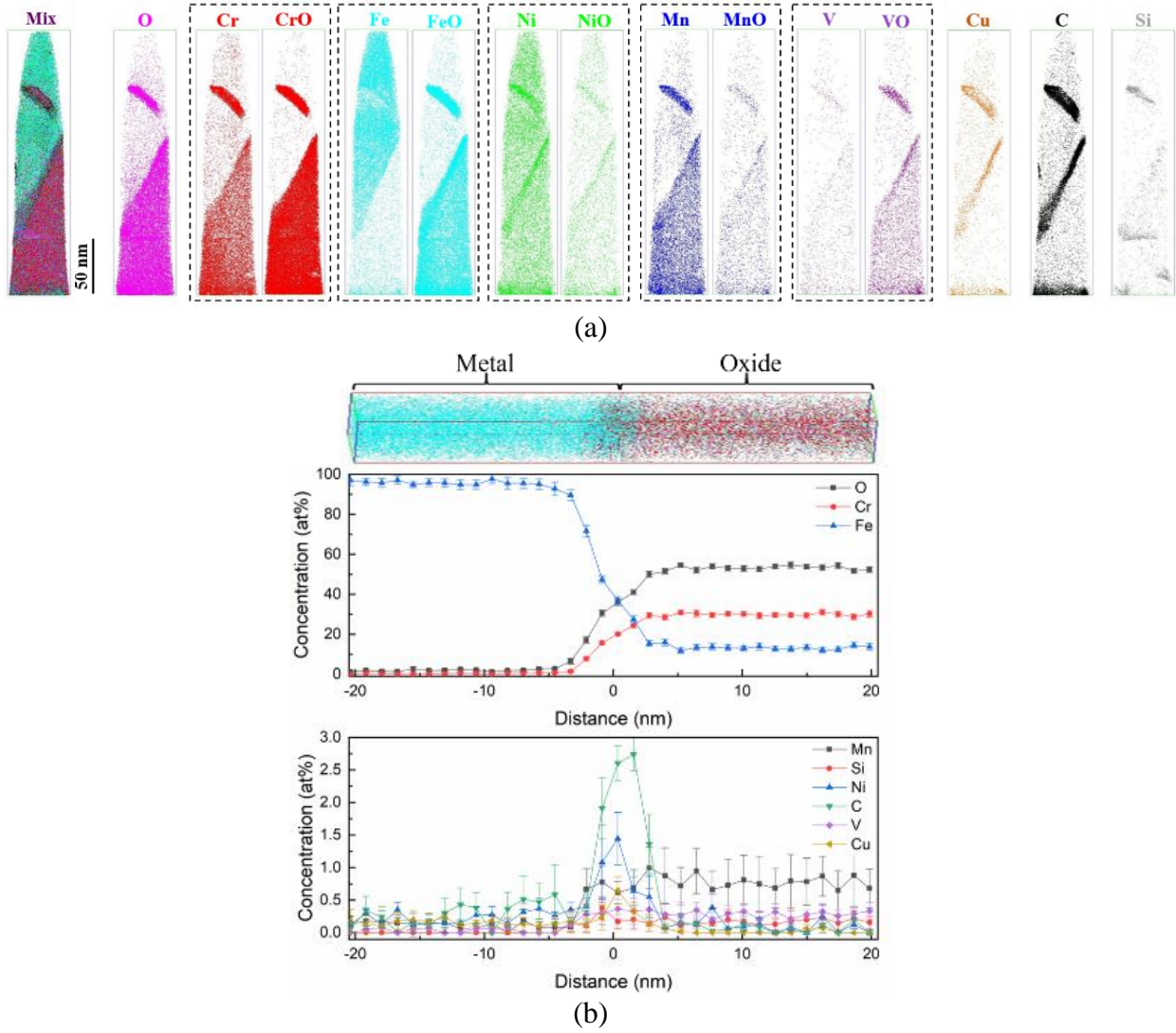


Fig. 15. (a) A representative region of Fe-9Cr ferritic steel showing ion distributions (plane thickness ~ 5 nm); (b) Line profiles showing the quantitative elemental distribution.

4. Discussion

4.1 The origin of different EBSD index rates in the internal oxide layer

The results shown in this and in our previous works [29, 31, 32, 87, 88] have shown the existence of an internal oxide layer in the two steels after exposure to SCW. Although the internal oxide layers in the two steels retain the same crystallographic information as the underneath unoxidized matrix (when they belong to a same grain), the index rate of the internal oxide layer of Fe-17Cr-9Ni steel is nearly the same with the underneath matrix while Fe-9Cr steel is much worse than the underneath matrix (Figs. 2 and 3). The worse index rate of the internal oxide layer of Fe-9Cr steel can be expected because the internal oxide layer consists of different crystallographic structures of the BCC matrix and FCC chromite (Fig. 5). The EBSD Kikuchi patterns are well indexed if the electron signal comes from a region (interaction volume) with a single phase. They cannot be well indexed when there are two or more phases present because the mixture of the Kikuchi patterns from the phases cannot be resolved by EBSD software. The nano-sized oxide phase is smaller than the electron interaction volume to be resolved by the EBSD. This is the reason why the oxide phase is not observed directly under EBSD analysis. Consequently, the EBSD unindexed pixels in the internal oxide layer of Fe-9Cr steel are

mainly originated from the overlap of the two phases. Although the mixture of the two phases in the internal oxide layer of Fe-17Cr-9Ni steel appears to be more intensive than that of Fe-9Cr steel, the index rate of this layer is even much better than the layer in Fe-9Cr steel. The ‘improved’ index rate is mainly originated from two factors. The first one is the Kikuchi patterns of the FCC austenite and the FCC chromite are too similar to be distinguished by the EBSD [25]. The second one is the identical crystallographic orientation of the two phases (Fig. 8). The Kikuchi pattern will be identified as FCC austenite or FCC chromite even if the electron beam hits a region where the two phases co-exist.

4.2 The effect of internal oxide morphology and phase boundary on the high-temperature oxidation

For the alloys serviced under high-temperature environments, it is critical to form a continuous, slow growing, thermodynamically stable oxide scale, which works as a barrier for elemental diffusion [83]. To achieve this purpose, a certain content of stable-oxide-forming elements such as Cr, Al, and Si, is required [84]. The minimum content of stable-oxide-forming elements is required for two reasons: 1) to achieve the transition from internal to external oxidation; and 2) to provide a diffusive flux of elements towards the oxide scale to enable its sustained growth and reformation in case of exfoliation. If the concentration of oxide-forming elements is lower than this critical value, a protective oxide scale cannot form and the internal oxidation may continue, which is the case of the two steels in this study (Fig. 3). The critical value of the stable-oxide-forming elements has been firstly calculated by Wagner [13], assuming that the internal oxide precipitates can block the inward flux of oxygen when the volume fraction of the internal oxides exceeds a certain value. A later study [61] for Al-In alloys shows that this critical volume fraction of internal oxide precipitates is about 30% above which the external oxidation can be assumed. This value has been widely used by the following researchers in the calculation of required critical concentration of oxide forming elements. However, recent studies [85, 86] show that this value is not a constant. It depends on factors such as the oxygen supersaturation, types of alloys, and the internal oxide morphology. The effect of oxygen supersaturation can be determined once the alloy and oxidation conditions are specified [87, 88], while the effect of internal oxide morphology is very complicated.

In Wagner’s original theory [13], the internal oxide precipitates are assumed to be spherical. In fact, the internal oxide precipitates are not spherical for most cases and with varied morphologies which depend on many factors [66]. The different morphologies could affect the inward flux of oxygen to different extents, and then affect the surface protective oxide formation. For example, needle-like precipitates may be more efficient in blocking the inward oxygen diffusion than spherical precipitates when they are oriented parallel to the specimen surface. On the contrary, if the needle-like precipitates are oriented perpendicular to the specimen surface, the blocking efficiency should be much lower than that of spherical precipitates. In addition, the phase boundary of the internal oxide precipitates and their surrounding matrix may work as fast-diffusion channels [89]. The extent of this diffusion enhancement of the phase boundaries depends on whether the phase boundaries are coherent or incoherent. If the phase boundary is incoherent and oriented perpendicular to the specimen surface, oxygen inward diffusion will be accelerated and therefore oxygen permeability will be increased. As a result, the kinetics of internal oxidation are enhanced, and the required critical concentration of oxide-forming elements is increased for the formation of a protective oxide scale.

The two steels in this study are good examples to show the complexity of the internal oxide precipitates under the same conditions. The internal oxide precipitates in Fe-17Cr-9Ni steel have near-spherical shape while they have needle-like shape in Fe-9Cr steel. The phase boundaries of the oxide precipitates and their surrounding matrix in Fe-17Cr-9Ni steel are semi-coherent (Fig. 8). The phase boundaries in

Fe-9Cr are more complicated. The longer side phase boundaries are coherent while the narrow side phase boundaries are incoherent (Figs. 10 and 11). In addition, these needle-like oxide precipitates are neither oriented parallel to the specimen surface nor perpendicular. As a result, the overall effect of these precipitates on oxygen permeability should take into account of both the morphology and distribution orientation of the internal oxide precipitates and phase boundary structure.

4.3 The factors affecting internal oxide morphology and phase boundary structure

As discussed above, both the internal oxide morphology and the structure of oxide-matrix phase boundary can affect the diffusion properties of both oxidant and cation, and therefore the critical value of Cr concentration for the formation of surface protective scale. Although a large number of internal oxide precipitates with different morphologies have been reported by many researchers [4, 5, 66], the underlying mechanisms controlling the morphologies of the internal oxide precipitates and the structure of oxide-matrix phase boundary have been scarcely reported. A fundamental understanding of this topic may provide new insights into the design of high-temperature corrosion-resistant alloys by controlling the internal oxide morphology and the structure of oxide-matrix phase boundary.

Although the two steels in this study were oxidized in the same environment and the internal oxide precipitates in the two steels are all identified as chromite, the crystallographic orientation relationships between the internal oxide precipitates and their surrounding matrix in the two steels are different. The internal oxide precipitates in Fe-17Cr-9Ni steel have the same crystallographic orientation with their surrounding matrix. Although the crystallographic orientation of the internal oxide precipitates in Fe-9Cr steel are different from their surrounding matrix, all the oxide precipitates have an identical crystallographic orientation relationship with their surrounding matrix, which has been shown to be $(001)_{\text{metal}} // (001)_{\text{oxide}}$ and $[001]_{\text{metal}} // [110]_{\text{oxide}}$ (Fig. 5). This orientation relationship has been widely reported in BCC-FCC systems, as described by the Baker-Nutting orientation relationship in literature, for example, the FCC TiC carbide and BCC Ti bearing steel [90] and FCC NbC carbide and BCC ferrite steel [91]. These results suggest that the crystallographic orientation of the newly formed internal oxide precipitates could be affected by the metal matrix. The biggest difference between the two steels, apart from their Cr content, is their matrix crystallographic structure: FCC in Fe-17Cr-9Ni steel and BCC in Fe-9Cr steel. The internal oxidation-induced chromite also has an FCC structure. Compared with Fe-9Cr, the crystallographic structure of FCC chromite appears to be more similar to FCC Fe-17Cr-9Ni steel. This may explain why the internal oxide precipitates in Fe-17Cr-9Ni steel retain the same crystallographic orientation with their surrounding matrix while they do not in Fe-9Cr steel. However, how the metal matrix determines the crystallographic orientation of the internal oxide precipitates remains unclear but should be related to the minimisation of the total alloy system energy.

The formation of internal oxide precipitates in metal matrix usually experiences two stages: nucleation and growth. If the nucleus grows at an equal rate in all directions, the internal oxide precipitates should have a spherical morphology. This is the case for the internal oxide precipitates in Fe-17Cr-9Ni steel, while those in Fe-9Cr steel seem to follow a different scenario. As discussed above, the crystallographic orientation of the newly formed internal oxide precipitates is determined by the metal matrix. Once a specific metal matrix is selected, the crystallographic orientation of the internal oxide precipitates in this matrix is fixed. In general, an incoherent interface has an interfacial energy larger than 0.5 J/m^2 , while the interfacial energy of a coherent interface is less than $0.01\text{--}0.2 \text{ J/m}^2$ [92]. It is widely reported that the growth of the precipitates on a coherent interface is much slower than on an incoherent interface [80–82]. The atomic-resolution imaging (Figs. 10 and 11) and related interface simulation (Fig. 13b) show that the longer side phase boundaries are coherent while the narrow side

phase boundaries are incoherent in Fe-9Cr steel. These results suggest that the growth rate of the oxide precipitates along different directions is not equal. A faster growth rate towards the narrow side than that towards the longer side will finally lead to the formation of needle-like morphology of internal oxide precipitates, which corresponds well with what was observed in Fe-9Cr steel. It is worth noting that since all the internal oxide precipitates in Fe-9Cr steel have the Baker-Nutting orientation relationship with their surrounding matrix, $(001)_{\text{metal}}// (001)_{\text{oxide}}$ phase boundaries always exist. It means that the slow growth interfaces always exist, which explains why all the internal oxide precipitates in Fe-9Cr steel always have a needle-like morphology. The atomic-resolution imaging (Fig. 8a) and related simulation (Fig. 13a) show that all phase boundaries in Fe-17Cr-9Ni steel have a semi-coherent structure. It means the internal oxide precipitates in Fe-17Cr-9Ni steel grow equally in all directions, which corresponds well with that observed in this steel.

As mentioned above, the internal oxide precipitates could inhibit the inward diffusion of oxygen. However, the interfaces between the internal oxide precipitates and their surrounding matrix may act as fast diffusion channels if the interface has an incoherent structure [89], which will, on the contrary, increase the overall inward oxygen diffusion. The results presented above show that the interface structure can be mainly affected by two factors: 1) crystallographic structures of the internal oxide precipitates and their surrounding metal matrix; and 2) the crystallographic orientation relationship between the two phases. Once this information is provided, the phase boundary structure could be obtained by the simulation method used in this study, which could save much effort compared with microscopic approach. In addition, by selecting appropriate base metal and internal oxide-forming element, there is potential to control the distribution, morphology, and interface structure of the internal oxide precipitates, in order to obtain better high-temperature corrosion-resistant materials.

4.4 The generation of stress during the internal oxidation

The formation of an IOZ in the two steels has been demonstrated to be due to the inward diffusion of oxygen and internal oxide precipitation [34, 36, 37, 68, 69]. Since the Pilling-Bedworth ratio of the internal oxide precipitates (chromite) was reported to be around 2.0 [93], the growth of the chromite precipitates in the metal matrix may introduce significant compressive stress. However, a large number of Fe ions diffuse outwards simultaneously to form a magnetite outer oxide layer. Hence, the loss of metallic Fe from the matrix may have (partially) released the stress caused by the growing of internal oxide. If the growth stress in the IOZ is completely compensated by the outward diffusion of Fe ions, the internal oxide layer will be free of stress. As a result, the stress in the IOZ is the competing result of internal oxide growth and outward Fe diffusion [94-96]. To examine this situation, a rough calculation was conducted for Fe-17Cr-9Ni steel under the same reaction condition but for a longer reaction time of 1500 h where an external Fe_3O_4 layer ($\sim 45 \mu\text{m}$ thick) and an IOZ ($60 \mu\text{m}$ thick) formed [34]. As evidenced in this work and also in [34], the internal oxides are FeCr_2O_4 spinel in the IOZ. If assuming all Cr elements in the IOZ are consumed in forming the FeCr_2O_4 oxide precipitates, then the volume change ΔV because of the internal oxide precipitation can be calculated. For one mole of alloy, ΔV , is given by

$$\Delta V = N_{\text{Cr}} V_{\text{CrFe0.5O2}} + N_{\text{FeNi}} V_{\text{FeNi}} - V_{\text{alloy}} \quad (1)$$

where N_i , V_i are the mole fractions and molar volumes of the indicated species. Approximating $V_{\text{FeNi}} \approx V_{\text{alloy}}$, then

$$\Delta V / V_{\text{alloy}} = N_{\text{Cr}} (V_{\text{CrFe0.5O2}} - V_{\text{alloy}}) / V_{\text{alloy}} \quad (2)$$

For this particular alloy, $N_{Cr} = 0.18$, $V_{alloy} = 7.1 \text{ cm}^3/\text{mol}$, and $V_{CrFe0.5O2} = 22.4 \text{ cm}^3/\text{mol}$ and it is found that $\Delta V/V_{alloy} = 0.39$. It means a large volume expansion about 39% occurs due to the internal oxide formation. This volume increase can be eliminated by outward Fe diffusion, forming Fe_3O_4 in external oxide layer. The volume of outer Fe_3O_4 can be calculated and converted to outward Fe volume as follows:

$$\Delta V_{Fe(outer)}/V_{inner} = (t_{Fe_3O_4} 3V_{Fe}/V_{Fe_3O_4})/t_{inner} \quad (3)$$

where $V_{Fe} = 7.1 \text{ cm}^3/\text{mol}$ and $V_{Fe_3O_4} = 46.4 \text{ cm}^3/\text{mol}$, and $t_{Fe_3O_4}$ and t_{inner} are thicknesses of outer Fe_3O_4 layer and inner oxide layer, respectively. As a result, $\Delta V_{Fe(outer)}/V_{inner} = 0.34$, which is close to $\Delta V/V_{alloy}$, implying that the volume increase resulting from internal oxidation can almost be accommodated by external Fe_3O_4 formation. This result is in line with the relatively flat outer-inner oxide layer interface observed in this work and in [34].

Although above success, it should be realised that the stress created could not all be eliminated at least locally. The vacancy formed because of Fe outward diffusion can be in the form of nano-porous structures [34] which is unable to effectively compensate the volume increase because of internal oxide precipitation. As a result, the internal stress can still be built up, in particularly in the area surrounding the oxide precipitates. In addition, the growth of internal oxide is not the only origin of the stress, the heteroepitaxy [97] and oxygen incorporation in substrate [98] may also contribute. The significant lattice distortion (Figs. 8 and 12) and preferential deformation (Fig. 6) in the matrix surrounding the internal oxide precipitates are very likely to be the result of local stress generated during the oxidation. The lattice distortion and preferential deformation could affect the subsequent metallic ions diffusion and oxygen lattice diffusion. This, in turn, will affect the accuracy of Wagner theory [13] predictions since the effect of stress is not considered. The effects of stress on high-temperature oxidation have been studied by many researchers [94, 96]. The related computational models to describe the oxidation–stress interaction process have also been widely reported [98–101]. The details about how the stress affects the high-temperature oxidation will not be discussed here and the interested readers can find a fuller discussion of this subject elsewhere [94, 98, 100, 101].

4.5 Effect of minor elements on internal oxide formation

The APT analysis in this work reveals the behaviour of minor alloying elements during the internal oxide formation. The results in Figs. 14 and 15 show that Mn and V are incorporated to the chromite, while Cu, C and Si are enriched along the chromite-matrix interface. This can be explained by both the solubility and the relatively high diffusion coefficients of Mn and V in chromite, as reported in [102]. The observation of Mn-oxide and/or V-oxide surmounted on the top of chromia scale provides evidence of this fast diffusion of Mn and/or V in oxide scale [103]. On the other hand, Cu, C and Si tend to accumulate at oxide-matrix interface. Clearly, the chromite is an effective barrier for the diffusion of these elements. The nucleation and growth of the internal oxides will repel these elements from the oxide to the interface because of very low solubilities of these elements in chromium-rich oxide [104]. This element enrichment at the interface may affect the growth of internal oxides, affecting their size and morphology.

It is worth noting that although the internal oxide precipitates in Fe-9Cr steel was observed to have a needle-like morphology, the oxide precipitates with other morphology were also observed (Fig. 3b). As mentioned above, the needle-like morphology was mainly attributed to the much slower growth rate at the $(001)_{oxide} // (001)_{BCC-metal}$ interface than that of $(1-10)_{oxide} // (100)_{BCC-metal}$ (Fig. 13). However, stress and the minor elements might also affect the morphology of the internal oxide precipitates (Figs.

12 and 15), which result in the formation of oxide precipitates with other morphology. Since most of the oxide precipitates were observed to have a needle-like morphology, the interface structure was believed to be the dominant factor that affecting the morphology of the internal oxide precipitates.

The above results have shown that there are potentials to tune the morphology of the internal oxide precipitates by adjusting the structure of the interface between the oxide precipitate and the matrix. Compared with the near-spherical precipitates, the formation of needle-like precipitates can be more efficient in preventing the inward oxygen diffusion if the growth direction of the needle-like precipitates was perpendicular to the direction of inward oxygen diffusion. Further research on this topic is required to obtain a comprehensive understanding on the potential approaches to control the preferential growth direction of the internal oxide precipitates with different morphologies.

5. Conclusions

The internal oxide precipitates in Fe-17Cr-9Ni steel have the same crystallographic orientation with their surrounding matrix. Although the internal oxide precipitates in Fe-9Cr steel do not have the same crystallographic orientation with their surrounding matrix, they have a specific crystallographic orientation relationship. This relationship was widely reported in BCC-FCC systems as Baker-Nutting orientation relationship. The internal oxide-matrix phase boundary in Fe-17Cr-9Ni steel always has a semi-coherent structure. The equal growth of the internal oxide precipitates in Fe-17Cr-9Ni steel in all directions is attributed to a near-spherical morphology. The Baker-Nutting orientation relationship between the oxide precipitates and their surrounding matrix indicates that the (001) plane of the two phases always parallel to each other. Since the structure of the $(001)_{\text{metal}}// (001)_{\text{oxide}}$ phase boundaries is coherent, the growth of the oxide precipitates on these boundaries is much slower than on other incoherent boundaries. This is the reason why the internal oxide precipitates in Fe-9Cr steel always have a needle-like morphology.

The internal oxide precipitation under the Pilling-Bedworth ratio conversion could introduce volume expansion. The outward diffusion of Fe ions to form the magnetite outer oxide layer could compensate the stress caused by the volume expansion. Hence, the property of the stress in the internal oxide layer is the competing result of internal oxide precipitation and outward Fe diffusion. A preliminary calculation for Fe-17Cr-9Ni steel shows that almost all volume increase due to internal oxide formation can be accommodated by outward Fe diffusion. However, the stress character in the IOZ could be variable during the oxidation process, which depends on the type of precipitates, cavity size, and morphology. Hence, the effect of stress on the high-temperature oxidation may also change during the oxidation process.

Acknowledgements

This work was financially supported by National Key Research and Development Program of China (No. 2018YFE0116200), Shanghai Pujiang Program (No. 21PJ1406400), and EPSRC (EP/K040375/1, EP/N010868/1, and EP/R009392/1). Prof. Lefu Zhang is acknowledged for providing the samples used in this study. Instrumental Analysis Center of SJTU is also gratefully acknowledged. The atom probe facilities at the University of Oxford are funded by the EPSRC (EP/M022803/1).

References

[1] C. Cabet, F. Dalle, E. Gaganidze, J. Henry, H. Tanigawa, Ferritic-martensitic steels for fission and fusion applications. *J. Nucl. Mater.*, 523(2019) 510-537.

- [2] I.G. Wright, R.B. Dooley, A review of the oxidation behaviour of structural alloys in steam. *Int. Mater. Rev.*, 55(2010) 129-167.
- [3] S.R.J. Saunders, M. Monteiro, F. Rizzo, The oxidation behaviour of metals and alloys at high temperatures in atmospheres containing water vapour: A review. *Prog. Mater. Sci.*, 53(2008) 775-837.
- [4] N. Birks, G.H. Meier, F.S. Pettit, *Introduction to the high temperature oxidation of metals*. Cambridge University Press, 2006.
- [5] D.J. Young, *High temperature oxidation and corrosion of metals*. Vol. 1., Elsevier, 2008.
- [6] T. Yang, X. Liu, X. Cheng. Optimization of multilayer fuel assemblies for supercritical water-cooled reactors with mixed neutron spectrum. *Nuclear engineering and design*, 249(2012) 159-165.
- [7] J. Hofmeister, C. Waata, J. Starflinger, T. Schulenberg, E. Laurien. Fuel assembly design study for a reactor with supercritical water. *Nuclear Engineering and Design*, 237(2007) 1513-1521.
- [8] R. Viswanathan, J. F. Henry, J. Tanzosh, G. Stanko, J. Shingledecker, B. Vitalis, R. Purgert. US program on materials technology for ultra-supercritical coal power plants. *Journal of materials engineering and performance* 14 (2005) 281-292.
- [9] Chunwen Sun, Rob Hui, Wei Qu, Sing Yick. Progress in corrosion resistant materials for supercritical water reactors. *Corrosion Science*, 51(2009): 2508-2523.
- [10] R. Viswanathan, J. Sarver, J.M. Tanzosh, Boiler materials for ultra-supercritical coal power plants—steam side oxidation. *J. Mater. Eng. Perform.*, 15(2006) 255-274.
- [11] F. Abe, Precipitate design for creep strengthening of 9% Cr tempered martensitic steel for ultra-supercritical power plants. *Sci. Technol. Adv. Mater.*, 9(2008) 013002.
- [12] S.J. Zinkle, G.S. Was, Materials challenges in nuclear energy. *Acta Mater.*, 61(2013) 735-758.
- [13] C. Wagner. Reaktionstypen bei der Oxydation von Legierungen, *Z. Elektrochem.*, 63 (1959) 772-782.
- [14] K. Chen, L. Zhang, Z. Shen, X. Zeng. Revealing the oxidation mechanism of 310S stainless steel in supercritical water via high-resolution characterization. *Corrosion Science*, 200(2022) 110212.
- [15] G.S. Was, P. Ampornrat, G. Gupta, S. Teyseyre, E.A. West, T.R. Allen, K. Sridharan, L. Tan, Y. Chen, X. Ren, C. Pister. Corrosion and stress corrosion cracking in supercritical water. *Journal of Nuclear Materials*, 371(2007) 176-201.
- [16] Z. Shen, J. Zhang, S. Wu, X. Luo, B.M. Jenkins, M.P. Moody, Sergio Lozano-Perez, X. Zeng. Microstructure understanding of high Cr-Ni austenitic steel corrosion in high-temperature steam. *Acta Materialia*, 226(2022) 117634.
- [17] X. Guo, Y. Fan, W. Gao, R. Tang, K. Chen, Z. Shen, L. Zhang. Corrosion resistance of candidate cladding materials for supercritical water reactor. *Annals of Nuclear Energy*, 127(2019) 351-363.
- [18] X. Luo, R. Tang, C. Long, Z. Miao, Q. Peng, C. Li. Corrosion behavior of austenitic and ferritic steels in supercritical water. *Nuclear Engineering and Technology*, 40(2008) 147-154.
- [19] X. Guo, K. Chen, W. Gao, Z. Shen, P. Lai, L. Zhang. A research on the corrosion and stress corrosion cracking susceptibility of 316L stainless steel exposed to supercritical water. *Corrosion Science*, 127(2017)157-167.
- [20] X. Guo, K. Chen, W. Gao, Z. Shen, L. Zhang. Corrosion behavior of alumina-forming and oxide dispersion strengthened austenitic 316 stainless steel in supercritical water. *Corrosion Science*, 138(2018) 297-306.
- [21] Z. Shen, L. Zhang, R. Tang, Q. Zhang. The effect of temperature on the SSRT behavior of austenitic stainless steels in SCW. *Journal of Nuclear Materials*, 454(2014) 274-282.
- [22] Z. Shen, L. Zhang, R. Tang, Q. Zhang. SCC susceptibility of type 316Ti stainless steel in supercritical water. *Journal of Nuclear Materials*, 458(2015) 206-215.

- [23] J. Ju, Z. Shen, M. Kang, J. Zhang, J. Wang. On the preferential grain boundary oxidation of a Ni-Co-based superalloy. *Corrosion Science*, 199(2022) 110203.
- [24] S.M. Li, L.B. Fu, W.L. Zhang, W. Li, J. Sun, T.G. Wang, S.M. Jiang, J. Gong, C. Sun. Formation process and oxidation behavior of MCrAlY+AlSiY composite coatings on a Ni-based superalloy. *Journal of Materials Science & Technology*, 120(2022) 65-77.
- [25] S. Zhang, H. Li, Z. Jiang, H. Feng, Z. Wen, J. Ren, P. Han. Unveiling the mechanism of yttrium significantly improving high-temperature oxidation resistance of super-austenitic stainless steel S32654. *Journal of Materials Science & Technology*, 115(2022) 103-114.
- [26] K. Chen, Z. Liu, X. Guo, H. Wang, Z. Shen, X. Zeng. Effect of surface finishing on the oxidation characteristics of a Fe-21Cr-32Ni alloy in supercritical carbon dioxide. *Corrosion Science*, 195(2022) 110019.
- [27] T.A. Listyawan, M.P. Agustianingrum, Y.S. Na, K.R. Lim, N. Park. Improving high-temperature oxidation behavior by modifying Al and Co content in Al-Co-Cr-Fe-Ni high-entropy alloy. *Journal of Materials Science & Technology*, 129(2022) 115-126.
- [28] S. Penttilä, A. Toivonen, J. Li, W. Zheng, R. Novotny. Effect of surface modification on the corrosion resistance of austenitic stainless steel 316L in supercritical water conditions. *The Journal of Supercritical Fluids*, 81(2013) 157-163.
- [29] X. Kong, W. Sun, Q. Wang, M. Chen, T. Zhang, F. Wang. Improving high-temperature wear resistance of NiCr matrix self-lubricating composites by controlling oxidation and surface texturing. *Journal of Materials Science & Technology*, 131(2022) 253-263.
- [30] G.S. Was, S. Teyseyre, Z. Jiao. Corrosion of austenitic alloys in supercritical water. *Corrosion*, 62(2006) 989-1005.
- [31] R. Novotny, P. Hähner, J. Siegl, P. Haušild, S. Ripplinger, S. Penttilä, A. Toivonen. Stress corrosion cracking susceptibility of austenitic stainless steels in supercritical water conditions. *Journal of Nuclear Materials*, 409(2011) 117-123.
- [32] X. Gao, X. Wu, Z. Zhang, H. Guan, E.H. Han. Characterization of oxide films grown on 316L stainless steel exposed to H₂O₂-containing supercritical water. *The Journal of supercritical fluids*, 42(2007) 157-163.
- [33] H. Chen, R. Tang, C. Long, G. Le. Effect of exposure temperature on the corrosion behaviors of TP347H austenitic stainless steel in supercritical water. *Corrosion Science*, 161(2019) 108188.
- [34] Z. Shen, D. Tweddle, H. Yu, G. He, A. Varambhia, P. Karamched, F. Hofmann, A.J. Wilkinson, M.P. Moody, L. Zhang, S. Lozano-Perez. Microstructural understanding of the oxidation of an austenitic stainless steel in high-temperature steam through advanced characterization. *Acta Materialia*, 194(2020) 321-336.
- [35] Y. Li, T. Xu, S. Wang, J. Yang, B. Fekete, J. Yang, A. Wu, J. Qiu, Y. Xu, D.D. Macdonald. Predictions and analyses on the growth behavior of oxide scales formed on ferritic–martensitic in supercritical water. *Oxidation of Metals*, 92(2019) 27-48.
- [36] Z. Shen, K. Chen, H. Yu, B. Jenkins, Y. Ren, N. Saravanan, G. He, X. Luo, P.A. Bagot, M.P. Moody, L. Zhang. New insights into the oxidation mechanisms of a Ferritic-Martensitic steel in high-temperature steam. *Acta Materialia*, 194(2020) 522-539.
- [37] K. Chen, L. Zhang, Z. Shen. Understanding the surface oxide evolution of T91 ferritic-martensitic steel in supercritical water through advanced characterization. *Acta Materialia*, 194(2020) 156-167.
- [38] L. Tan, X. Ren, T.R. Allen. Corrosion behavior of 9–12% Cr ferritic–martensitic steels in supercritical water. *Corrosion science*, 52(2010) 1520-1528.
- [39] Y. Chen, K. Sridharan, T. Allen. Corrosion behavior of ferritic–martensitic steel T91 in supercritical water. *Corrosion Science*, 48(2006) 2843-2854.

- [40] K. Yin, S. Qiu, R. Tang, Q. Zhang, L. Zhang. Corrosion behavior of ferritic/martensitic steel P92 in supercritical water. *The Journal of Supercritical Fluids*, 50(2009) 235-239.
- [41] L. Tan, M.T. Machut, K. Sridharan, T.R. Allen. Corrosion behavior of a ferritic/martensitic steel HCM12A exposed to harsh environments. *Journal of Nuclear Materials*, 371(2007) 161-170.
- [42] J. Bischoff, A.T. Motta. Oxidation behavior of ferritic–martensitic and ODS steels in supercritical water. *Journal of Nuclear Materials*, 424(2012) 261-276.
- [43] J. Bischoff, A.T. Motta. EFTEM and EELS analysis of the oxide layer formed on HCM12A exposed to SCW. *Journal of nuclear materials*, 430(2012) 171-180.
- [44] I. Betova, M. Bojinov, P. Kinnunen, V. Lehtovuori, S. Peltonen, S. Penttilä, T. Saario. Composition, structure, and properties of corrosion layers on ferritic and austenitic steels in ultrasupercritical water. *Journal of the Electrochemical Society*, 153(2006) B464.
- [45] L. Sun, W.P. Yan. Estimation of oxidation kinetics and oxide scale void position of ferritic-martensitic steels in supercritical water. *Adv. Mater. Sci. Eng.* (2017) 1-12.
- [46] N.Q. Zhang, H. Xu, B.R. Li, Y. Bai, D.Y. Liu. Influence of the dissolved oxygen content on corrosion of the ferritic–martensitic steel P92 in supercritical water. *Corrosion science*, 56(2012) 123-128.
- [47] J. Bischoff, A.T. Motta, C. Eichfeld, R.J. Comstock, G. Cao, T.R. Allen. Corrosion of ferritic–martensitic steels in steam and supercritical water. *Journal of Nuclear Materials*, 441(2013) 604-611.
- [48] L. Tan, Y. Yang, T.R. Allen. Oxidation behavior of iron-based alloy HCM12A exposed in supercritical water. *Corrosion Science*, 48(2006) 3123-3138.
- [49] J. Bischoff, A.T. Motta, R.J. Comstock. Evolution of the oxide structure of 9CrODS steel exposed to supercritical water. *Journal of Nuclear Materials*, 392(2009) 272-279.
- [50] X. Zhong, X. Wu, E.H. Han. Effects of exposure temperature and time on corrosion behavior of a ferritic–martensitic steel P92 in aerated supercritical water. *Corrosion Science*, 90(2015) 511-521.
- [51] Z. Zhu, H. Xu, D. Jiang, X. Mao, N. Zhang. Influence of temperature on the oxidation behaviour of a ferritic-martensitic steel in supercritical water. *Corrosion Science*, 113(2016) 172-179.
- [52] X. Zhong, X. Wu, E.H. Han. The characteristic of oxide scales on T91 tube after long-term service in an ultra-supercritical coal power plant. *The Journal of Supercritical Fluids*, 72(2012) 68-77.
- [53] Z. Shen, K. Chen, X. Guo, L. Zhang. A study on the corrosion and stress corrosion cracking susceptibility of 310-ODS steel in supercritical water. *Journal of Nuclear Materials*, 514(2019) 56-65.
- [54] K. Li, Z. Wang, K. Song, K. Khanlari, X.S. Yang, Q. Shi, X. Liu, X. Mao. Additive manufacturing of a Co-Cr-W alloy by selective laser melting: In-situ oxidation, precipitation and the corresponding strengthening effects. *Journal of Materials Science & Technology*, 125(2022) 171-181.
- [55] H. Hu, Z. Zhou, M. Li, L. Zhang, M. Wang, S. Li, C. Ge. Study of the corrosion behavior of a 18Cr-oxide dispersion strengthened steel in supercritical water. *Corrosion science*, 65(2012) 209-213.
- [56] A. Atkinson, R.I. Taylor. ⁵⁵Fe and ¹⁸O tracers in magnetite scales growing on iron and dilute iron-silicon alloys. *High Temperatures. High Pressures (Print)*, 14(1982)c571-580.
- [57] A.M. Pritchard, N.E.W. Hartley, J.F. Singleton, A.E. Truswell. Oxygen-18 and deuterium profiling in thick films on Fe-9% Cr alloys by 3 MeV nuclear microprobe. *Corrosion Science*, 20(1980) 1-17.
- [58] M.R. Taylor, J.M. Calvert, D.G. Lees, D.B. Meadowcroft. The mechanism of corrosion of Fe-9% Cr alloys in carbon dioxide. *Oxidation of Metals*, 14(1980) 499-516.
- [59] J. Robertson, M. I. Manning. Criteria for formation of single layer, duplex, and breakaway scales on steels. *Materials Science and Technology*, 4(1988) 1064-1071.
- [60] F. H. Stott, G. C. Wood. Internal oxidation. *Materials Science and Technology*, 4(1988) 1072-1078.

- [61] R.A. Rapp. Kinetics, microstructures and mechanism of internal oxidation-its effect and prevention in high temperature alloy oxidation. *Corrosion*, 21(1965) 382-401.
- [62] N. Otsuka, Y. Shida, H. Fujikawa. Internal-external transition for the oxidation of Fe-Cr-Ni austenitic stainless steels in steam. *Oxidation of Metals*, 32(1989) 13-45.
- [63] R. C. Newman, F. Scenini. Another way to think about the critical oxide volume fraction for the internal-to-external oxidation transition?. *Corrosion*, 64(2008) 721-726.
- [64] W. Zhao, Y. Kang, J. M. A. Orozco, B. Gleeson. Quantitative approach for determining the critical volume fraction for the transition from internal to external oxidation. *Oxidation of Metals*, 83(2015) 187-201.
- [65] D.P. Whittle, Y. Shida, G.C. Wood, F.H. Stott, B.D. Bastow. Enhanced diffusion of oxygen during internal oxidation of nickel-base alloys. *Philosophical Magazine A*, 46(1982) 931-949.
- [66] D. L. Douglass. A critique of internal oxidation in alloys during the post-Wagner era. *Oxidation of Metals*, 44(1995) 81-111.
- [67] D. J. Young. Predicting internal oxidation: building on the Wagner model. *Materials Science Forum*, 696(2011) 1-11.
- [68] K. Chen, L. Zhang, S. Wu, Z. Shen. High-resolution characterization of the internal and external oxidation of austenitic alloys in supercritical water. *Scripta Materialia*, 197(2021) 113814.
- [69] D. Du, K. Chen, L. Zhang, Z. Shen. Microstructural investigation of the nodular corrosion of 304NG stainless steel in supercritical water. *Corrosion Science*, 170(2020) 108652.
- [70] L. Luo, M. Su, P. Yan, L. Zou, D.K. Schreiber, D.R. Baer, Z. Zhu, G. Zhou, Y. Wang, S.M. Bruemmer, Z. Xu. Atomic origins of water-vapour-promoted alloy oxidation. *Nature materials*, 17(2018) 514-518.
- [71] D.G. Xie, Z.J. Wang, J. Sun, J. Li, E. Ma, Z.W. Shan. In situ study of the initiation of hydrogen bubbles at the aluminium metal/oxide interface. *Nature materials*, 14(2015)c899-903.
- [72] A. King, G. Johnson, D. Engelberg, W. Ludwig, J. Marrow. Observations of intergranular stress corrosion cracking in a grain-mapped polycrystal. *Science*, 321(2008) 382-385.
- [73] T.L. Burnett, P.J. Withers. Completing the picture through correlative characterization. *Nature Materials*, 18(2019) 1041-1049.
- [74] A. J. Wilkinson, D. Randman. Determination of elastic strain fields and geometrically necessary dislocation distributions near nanoindents using electron back scatter diffraction. *Philosophical Magazine*, 90(2010) 1159-1177.
- [75] W. Pantleon. Resolving the geometrically necessary dislocation content by conventional electron backscattering diffraction. *Scripta Materialia*, 58(2008) 994-997.
- [76] J.F. Nye. Some geometrical relations in dislocated crystals. *Acta Metallurgica*, 1(1953) 153-162.
- [77] P.J. Konijnenberg, S. Zaefferer, D. Raabe. Assessment of geometrically necessary dislocation levels derived by 3D EBSD. *Acta Materialia*, 99(2015) 402-414.
- [78] M.J. Hÿtch, E. Snoeck, R. Kilaas. Quantitative measurement of displacement and strain fields from HREM micrographs. *Ultramicroscopy*, 74(1998) 131-146.
- [79] A. Pratt, L. Lari, O. Hovorka, A. Shah, C. Woffinden, S.P. Tear, C. Binns, R. Kröger. Enhanced oxidation of nanoparticles through strain-mediated ionic transport. *Nature materials*, 13(2014) 26-30.
- [80] T. Chen, J.G. Gigax, L. Price, D. Chen, S. Ukai, E. Aydogan, S.A. Maloy, F.A. Garner, L. Shao. Temperature dependent dispersoid stability in ion-irradiated ferritic-martensitic dual-phase oxide-dispersion-strengthened alloy: Coherent interfaces vs. incoherent interfaces. *Acta Materialia*, 116(2016) 29-42.

- [81] J.W. Bai, P.P. Liu, Y.M. Zhu, X.M. Li, C.Y. Chi, H.Y. Yu, X.S. Xie, Q. Zhan. Coherent precipitation of copper in Super304H austenite steel. *Materials Science and Engineering: A*, 584(2013) 57-62.
- [82] B. Appolaire, E. Aeby-Gautier, J.D.C. Teixeira, M. Dehmas, S. Denis. Non-coherent interfaces in diffuse interface models. *Philosophical Magazine*, 90(2010) 461-483.
- [83] D. Jullian, A. Prillieux, J. Zhang, D.J. Young. Oxygen permeability of Fe - Ni - Cr alloys at 1100 and 1150° C under carbon - free and carbon - containing gases. *Materials and Corrosion*, 68(2017) 197-204.
- [84] L.S. Darken. Some Observation on Atoms and Imperfection. *Transactions of the ASM*, 54(1961) 600-642.
- [85] J.B. Leblond. A note on a nonlinear version of Wagner's classical model of internal oxidation. *Oxidation of metals*, 75(2011) 93-101.
- [86] W. Zhao, Y. Kang, J.M.A. Orozco, B. Gleeson. Quantitative approach for determining the critical volume fraction for the transition from internal to external oxidation. *Oxidation of Metals*, 83(2015) 187-201.
- [87] G. Böhm, M. Kahlweit. Über die innere Oxydation von Metallegierungen. *Acta Metallurgica*, 12(1964) 641-648.
- [88] F. Gesmundo, P. Castello, F. Viani, C. Roos. The effect of supersaturation on the internal oxidation of binary alloys. *Oxidation of metals*, 49(1998) 237-260.
- [89] A. Martinez-Villafane, F.H. Stott, J.G. Chacon-Nava, G.C. Wood. Enhanced oxygen diffusion along internal oxide-metal matrix interfaces in Ni-Al alloys during internal oxidation. *Oxidation of metals*, 57(2002) 267-279.
- [90] H.W. Yen, C.Y. Chen, T.Y. Wang, C.Y. Huang, J.R. Yang. Orientation relationship transition of nanometre sized interphase precipitated TiC carbides in Ti bearing steel, *Mater. Sci. Tech-Lond.*, 26 (2010) 421-430.
- [91] S. Shanmugam, R.D.K. Misra, T. Mannering, D. Panda, S.G. Jansto, Impact toughness and microstructure relationship in niobium-and vanadium-microalloyed steels processed with varied cooling rates to similar yield strength, *Mater. Sci. Eng. A-Struct.*, 437 (2006) 436-445.
- [92] D.A. Porter, K.E. Easterling. *Phase Transformations in Metals and Alloys*, Chapman & Hall, London (1992).
- [93] T. Terachi, T. Yamada, T. Miyamoto, K. Arioka, K. Fukuya. Corrosion behavior of stainless steels in simulated PWR primary water—effect of chromium content in alloys and dissolved hydrogen—. *Journal of nuclear science and technology*, 45(2008) 975-984.
- [94] H.E. Evans. Stress effects in high temperature oxidation of metals. *International materials reviews*, 40(1995) 1-40.
- [95] H. Zhou, J. Qu, M. Cherkaoui. Stress-oxidation interaction in selective oxidation of Cr-Fe alloys. *Mechanics of Materials*, 42(2010) 63-71.
- [96] L. Bradley, G.C. Wood, F.H. Stott. The effects of stress on the internal oxidation of Ni-Cr and Ni-Al alloys. In *Materials science forum*, 251(1997) 341-348.
- [97] B. Pieraggi, R.A. Rapp. Stress generation and vacancy annihilation during scale growth limited by cation-vacancy diffusion. *Acta Metallurgica*, 36(1988) 1281-1289.
- [98] S. Guruswamy, S. M. Park, J. P. Hirth, R. A. Rapp. Internal oxidation of Ag-In alloys: stress relief and the influence of imposed strain. *Oxidation of Metals*, 26(1986) 77-100.
- [99] A.M. Huntz. Stresses in NiO, Cr₂O₃ and Al₂O₃ oxide scales. *Materials Science and Engineering: A*, 201(1995) 211-228.

- [100] D.R. Clarke. The lateral growth strain accompanying the formation of a thermally grown oxide. *Acta Materialia*, 51(2003) 1393-1407.
- [101] A.M. Limarga, D.S. Wilkinson, G.C. Weatherly. Modeling of oxidation-induced growth stresses. *Scripta Materialia*, 50(2004) 1475-1479.
- [102] A. Naoumidis, H.A. Schulze, W. Jungen, P. Lersch. Phase studies in the chromium-manganese-titanium oxide system at different oxygen partial pressures. *Journal of the European Ceramic Society*, 7(1991) 55-63.
- [103] T.D. Nguyen, J. Zhang, D.J. Young. Effect of Mn on oxide formation by Fe-Cr and Fe-Cr-Ni alloys in dry and wet CO₂ gases at 650° C. *Corrosion Science*, 112(2016) 110-127.
- [104] H.J. Grabke, I. Wolf. Carburization and oxidation. *Materials Science and Engineering*, 87(1987) 23-33.